Quantum state transfer and maximal entanglement between distant qubits using a minimal quasicrystal pump

Arnob Kumar Ghosh [1,*] Rubén Seoane Souto [2] Vahid Azimi-Mousolou [1]
Annica M. Black-Schaffer [1,†,‡] and Patric Holmvall [1,†,§]
[1] *Department of Physics and Astronomy, Uppsala University, Box 516, 75120 Uppsala, Sweden*
[2] *Instituto de Ciencia de Materiales de Madrid (ICMM), Consejo Superior de Investigaciones Científicas (CSIC), Sor Juana Inés de la Cruz 3, 28049 Madrid, Spain*

(Received 23 July 2025; revised 12 August 2025; accepted 6 November 2025; published 26 November 2025)

Coherent quantum state transfer over macroscopic distances between non-neighboring elements in quantum circuits is a crucial component to increase connectivity and simplify quantum information processing. To facilitate such transfers, an efficient and easily controllable quantum pump would be highly beneficial. In this work, we demonstrate such a quantum pump based on a one-dimensional quasicrystal Fibonacci chain (FC). In particular, we utilize the unique properties of quasicrystals to pump the edge-localized winding states between the two distant ends of the chain by only minimal manipulation of the FC at its end points. We establish the necessary conditions for successful state transfer within a fully time-dependent picture and also demonstrate robustness of the transfer protocol against disorder. We then couple external qubits to each end of the FC and establish highly adaptable functionality as a quantum bus with both on-demand switching of the qubit states and generation of maximally entangled Bell states between the qubits. Thanks to the minimal control parameters, the setup is well-suited for implementation across diverse experimental platforms, thus establishing quasicrystals as an efficient platform for versatile quantum information processing.

DOI: 10.1103/8zys-w2v4

I. INTRODUCTION

Reliable transfer of quantum states and the distribution of entanglement over macroscopic distances [1,2] are central in emerging quantum technologies. This includes secure quantum communication and distributed quantum computing [3–8], underlying the development of the quantum internet, aimed at interconnecting quantum processors across extensive distances [9–11]. Key to this endeavor are quantum buses capable of reversibly entangling and transferring quantum information between physical systems. Various physical platforms have already been proposed, including atoms coupled to cavities [12,13], quantum spin chains [14–16], and phononic systems [17]. However, these protocols often face challenges from disorder and noise, which degrade fidelity and hinder scalability.

A quantum pump based on protected boundary states of a topological material [18–20] can lead to topological quantum state transfer [21], which is naturally robust to disorder. To this end, quantum state transfer has already been proposed in several different topological systems [22–49]. For example, there exist theory proposals for quantum state transfer based on the chiral edge state in quantum spin liquids [23,26], but facing substantial experimental challenges. A much larger set of work has instead focused on topological quantum state transfer in the dimerized Su–Schrieffer–Heeger (SSH) model [25,27–38,40–49], which is the simplest one-dimensional (1D) topological setup and a periodic system. However, state transfer in an SSH chain is only achieved by dynamically switching the bond strength between intracell and intercell sites throughout the whole system [25,28–38,40–49]. This leads to the number of operations to achieve a state transfer growing linearly with the distance, again limiting experimental feasibility. Here, we instead identify a 1D quasicrystal as a simpler and more efficient platform for achieving topological quantum state transfer, often not needing more than one or two bond switches in total, despite long distances.

Quasicrystals are quasiperiodic materials without translational symmetry but with exotic properties, such as discrete scale invariance and multifractal energy spectrum [50–60]. One of the most well-studied quasicrystals is the 1D Fibonacci chain (FC) [61,62], which contains quasiperiodic modulation of either the hopping strength or on-site potential, following the Fibonacci sequence [61,62]. Interestingly, the 1D FC can be associated with the topological properties of a two-dimensional (2D) crystal Chern insulator under the inclusion of a so-called phason degree of freedom [61–69]. The resulting Chern numbers are associated with gap labels for

*Contact author: arnob.ghosh@physics.uu.se
†These authors contributed equally to this work.
‡Contact author: annica.black-schaffer@physics.uu.se
§Contact author: patric.holmvall@physics.uu.se

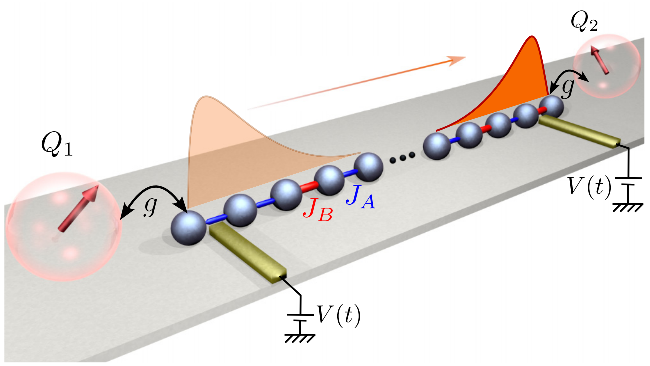

FIG. 1. The FQP consists of an FC with weak bonds J_A (blue) and strong bonds J_B (red). The transfer protocol $V(t)$ dynamically modifies the outermost bonds of the FC and induces a transfer of a winding state from the left end (light orange) to the right (dark orange). External qubits Q_1 and Q_2 are coupled to the FQP with coupling constant g. The FQP can transfer a state between the two qubits or generate maximally entangled states between them.

each quasicrystal energy gap, which has been demonstrated in diffraction experiments [70]. Subsequently, the FC supports topologically protected in-gap edge-localized states that 'wind' inside the quasicrystal gap, with a winding number equal to the gap label of that gap [61,62]. These winding states have also been employed for quantum state transfer in photonic quasicrystals [22,24] and optical setups [71]. However, previous work has not provided any protocol for on-demand transfer and, especially, demanded protocols that requires bond strengths to be switched throughout the whole length of the quasicrystal [22,24,71], which results in a similarly cumbersome setup as for the SSH chain [25,28–38,40–49]. Finding a protocol that requires only minimal parameter switches for topological quantum state transfer, also over longer distances, is therefore absolutely crucial for any feasible and on-demand experimental realizations. Moreover, an important outstanding goal is to demonstrate that such a quantum pump can, in fact, be used for other important tasks such as entanglement generation and state preparation, paving the way to general-purpose quantum information processing.

In this work, we exploit the intriguing quasiperiodic properties of the FC to develop a minimal topological Fibonacci quantum pump (FQP), which requires only switching of one or two of the outermost bonds of the FC; see Fig. 1 for an illustration. This dramatically reduces complexity and allows for simple and efficient implementation in different experimental frameworks, not just limited to optical setups [22,24,71] but also feasible with superconducting resonators [72], Josephson junction arrays [73], or mechanical systems [39]. In particular, by studying the full-time evolution, we show how quantum state transfer is readily achieved with the FQP for a wide range of parameters and several simple transfer protocols. Importantly, we then utilize the FQP as a quantum bus to transmit information between two distant qubits connected at each end of the pump (see Fig. 1) and demonstrate both complete quantum state transfer and how to create maximally entangled Bell states between the qubits. Thus, the FQP may be controlled on demand for a variety of applications.

The remainder of the paper is organized as follows. In Sec. II, we discuss the properties of the Fibonacci chain, which act as the building block of the pump. In Sec. III, we demonstrate the pumping of the winding states in the FQP. In Sec. IV, we employ the FQP to transfer and create maximal entanglement between two distant qubits. We conclude with a summary and discussion in Sec. V.

II. BACKGROUND: FIBONACCI CHAIN

The 1D FC can be modeled by the Hamiltonian [61]

$$H = \mu \sum_i c_i^\dagger c_i + \sum_i J_i c_i^\dagger c_{i+1} + \text{H.c.}, \tag{1}$$

where μ represents the chemical potential, $c_i^\dagger$ is the electronic creation operator at lattice site i, and J_i is either a weak (J_A) or a strong (J_B) bond between two nearest-neighbor sites, with $\{J_i\}$ belonging to the Fibonacci sequence $\{C_n\}$. Here the nth Fibonacci approximant C_n is constructed through the concatenation rule $C_n = C_{n-1} \oplus C_{n-2}$ ($\forall n \geqslant 2$), with $C_0 = J_B$ and $C_1 = J_A$, leading to $C_2 = J_A J_B$, $C_3 = J_A J_B J_A$, $C_4 = J_A J_B J_A J_A J_B$, etc. [61]. Thus, the total number of bonds N_B in C_n is given by the Fibonacci number $F_n = F_{n-1} + F_{n-2}$, $\forall n \geqslant 2$, with $F_0 = F_1 = 1$. Longer Fibonacci chains can also be constructed by repeating l times the approximant C_n, such that the number of lattice sites is $L = lF_n + 1$. We here always employ open boundary conditions (OBCs) for the chain, set $J_A = 1$, $\mu = 0$, and consider the dimensionless hopping ratio $\rho = J_B/J_A$. All energies (and times) are thus given in units of J_A. We verify that other parameters give qualitatively the same results. We also consider natural units, such that $c = \hbar = 1$.

The FC can alternatively be constructed using the sign of a characteristic function χ_i, such that positive (negative) values of χ_i set the ith bond strength to J_B (J_A) [61], with $\chi_i = \text{sgn}[\cos(2\pi i \tau^{-1} + \pi\tau^{-1} + \phi) - \cos(\pi\tau^{-1})]$, where $\tau = (1+\sqrt{5})/2$ is the golden ratio and $\phi \in [0, 2\pi)$ the phason angle. Changes in the phason angle account for pairwise flipping of specific bond strengths [74] and as the phason angle ϕ varies from 0 to 2π, the topologically protected states wind across the energy gap [63]. We illustrate this in Fig. 2(a) for a C_8 FC, where two in-gap states (red and black lines) wind once through one of the larger gaps (gray shaded) and are separated from the remaining states (blue lines). These states are therefore often referred to as winding states. The number of windings inside a specific energy gap is equal to its gap label, which can be connected to the Chern number of a parent 2D system using also the phasonic degree of freedom [61–69]. The winding states with energies inside the gap are localized at one end of the FC, while they delocalize when approaching the gap edge [63]. In Fig. 2(a), $\mathcal{C} = 1$ for the highlighted winding states.

To construct an FQP with only small and easily implementable changes to the FC, we identify nearby values of the phason angle ϕ that amount to only flipping two outermost bonds in an FC approximant. This occurs, for example, for angles ϕ_1 (green dashed line) and ϕ_2 (orange dashed line) in Fig. 2(a), with the change of the outermost bonds indicated by arrows in Fig. 2(b). We then identify a large gap with a winding state well-separated from other states at these two phason angles as the state to pump, here the red winding

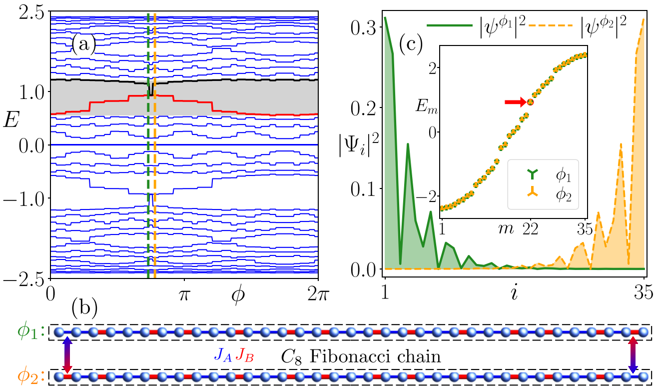

FIG. 2. (a) Eigenvalues E as a function of phason angle ϕ. Red and black curves represent winding states in one of the larger quasicrystal energy gaps (gray shaded). (b) Flipping between strong (red) and weak (blue) bonds indicated by arrows, when changing phason angle from ϕ_1 (green) to ϕ_2 (orange), also marked in (a). (c) Spatially resolved amplitude of the red winding state along the chain at ϕ_1 (green) and ϕ_2 (orange). Inset shows the eigenvalue spectrum E_m as a function of the state index m for phason angles ϕ_1 (green) and ϕ_2 (orange), with red dot and arrow marking the winding state. Here we use a C_8 FC with $L = F_8 + 1 = 35$ sites and $\rho = 1.5$, $\phi_1 = 0.73\pi$, and $\phi_2 = 0.78\pi$.

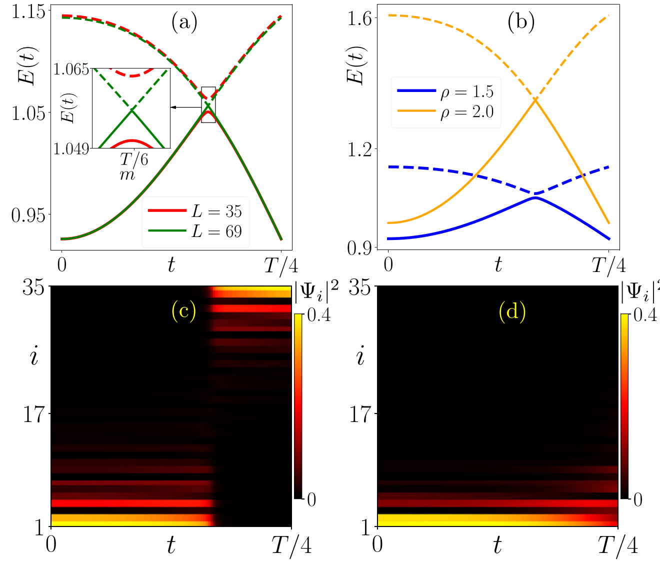

FIG. 3. (a) Eigenvalue evolution $E(t)$ of the winding state (solid) and the next excited state (dashed) as a function of time t for the C_8 FC with $L = F_8 + 1 = 35$ (red) and $L = 2F_8 + 1 = 69$ (green). Inset shows enlarged excitation gap. Here $\rho = 1.5$. (b) Same as (a) but for different hopping ratios $\rho = 1.5$ (blue) and 2.0 (orange) for the FC $L = F_8 + 1 = 35$. (c) Evolution of the winding state as a function of time t and spatial position i for $\rho = 1.5$ for the FC $L = F_8 + 1 = 35$. (d) Same as (c) but for $\rho = 2.0$. In all panels, the transfer rate is $\Omega = 10^{-4}$.

state in Fig. 2(a). In Fig. 2(c), we plot the eigenstate of this winding state at phason angle ϕ_1 (green) and find that it is well localized at the left side of the FC, while for the ϕ_2 angle (orange), its localization is completely switched to the right side. This change of localization of the winding state is the key component for using the FC as a quantum pump. Generally, such a pair of phason angles is always possible to identify and occurs for angles on either side of a critical angle ϕ_c where the winding state (red) approaches another winding state (black); see Fig. 2(a). The black winding state can also be employed as a pumping state, but with worse performance due to less edge localization. Instead, the black state often becomes the lowest excited state during the transfer. Moreover, all eigenvalues corresponding to the ϕ_1 and ϕ_2 FCs are unchanged since they are symmetrically oriented around ϕ_c; see inset in Fig. 2(c). Importantly, we only need to switch the two outermost bonds in order to go from phason angle ϕ_1 to ϕ_2 via ϕ_c and thereby obtain well-localized winding states at different ends of the chain, making it experimentally simpler than SSH-type topological pumps [25,28–38,40–49] or earlier suggested FC pumps [22,24,71].

III. MINIMAL TOPOLOGICAL PUMP

Next, we demonstrate pumping of FC winding states. We focus on the C_8 FC in Fig. 3 in the main text, but other approximants of FCs show similar results; see Appendix B. We consider the state to be initialized (at time $t = 0$) as the edge-localized winding state $\psi_w(0) = \psi_w^{\phi_1}$ at the left end of the chain for hopping sequence $\{J_i^{\phi_1}\}$ given by phason angle ϕ_1; see green state in Fig. 2(c). We then apply an adiabatic one-step transfer protocol that switches only the two outermost bonds, marked by arrows in Fig. 2(b), such that we end up with the phason angle ϕ_2 FC.[1] The explicit time dependence of the hopping is given in Eq. (A1) in Appendix A 1, with adiabaticity controlled by the rate Ω and illustrated in the inset of Fig. 5(a). We solve explicitly for the full time dependence to accurately capture the transfer, including nonadiabatic effects; see Appendix A 2.

To maintain adiabatic evolution and thus achieve complete state transfer, the winding state needs to have a finite excitation gap separating it from all other excited states. Otherwise, if the excitation gap is too small or the rate Ω too high, the winding state may make a transition, ending up in the excited level, which results in no clean state transfer and broken adiabaticity [29,75]. We therefore, in Figs. 3(a) and 3(b), investigate the evolution of the energies of the winding state (solid) and the next excited state (dashed). As seen in Fig. 3(a), the excitation gap decreases as we increase the number of repetitions of approximants from $L = F_8 + 1 = 35$ (red) to $L = 2F_8 + 1 = 69$ (green). We can instead consider other approximants, but find also then that the excitation gap decreases with increased chain length, see Appendix B. We thus attribute the existence of an excitation gap to a finite size effect, also in agreement with earlier results [75]. In addition, we investigate the effect of the hopping ratio ρ on the excitation gap size in Fig. 3(b). Here, the excitation gap diminishes with increasing ρ. We thus need to consider an appropriate

[1]For a short approximant, we may need to repeat the approximant more than once to obtain a desired system size, which then requires changing two bonds per repetition.

system size and hopping ratio to keep a finite excitation gap and thus adiabaticity.

We illustrate the importance of adiabaticity in Figs. 3(c) and 3(d), where we plot the transfer of the winding state for different ρ. Here, a smaller (larger) value of ρ yields a larger (smaller) excitation gap and leads to a successful (unsuccessful) FQP operation for a given transfer rate Ω. In the former case, the state gets transferred completely to the other end of the system, following an adiabatic evolution, while in the latter case, the state remains on the same side as the initial state due to loss of adiabaticity. Furthermore, the FQP operation is also robust against both on-site and bond disorder; see Appendix C. For efficient, fast, and successful on-demand FQP operations, it is therefore essential to find optimum conditions based on controllable parameters.

To capture the performance of the FQP quantitatively, we define a weighted fidelity $\bar{\mathcal{F}}$ (see Appendix A 3), which measures the overlap between the time-evolved state $\psi(t_f)$ at the end of the protocol at $t = t_f$ and a target state $\psi_{\rm T} = \psi_w^{\phi_2}$, i.e., the winding state for ϕ_2 [orange state in Fig. 2(c)]. The fidelity is also weighted by a factor α that ensures that the target state is an edge state localized at the right end of the chain see Eq. (A5) in Appendix A 3. Thus, $\bar{\mathcal{F}} \simeq 1$ indicates a successful transfer of states to the other end of the FC. We plot $\bar{\mathcal{F}}$ in Fig. 4(a) as a function of hopping ratio ρ and rate Ω for the C_8 FC. For $\rho = 1$, the fidelity is zero since the system is conventional 1D metal with no edge states. But as soon as the system becomes a quasicrystal, the fidelity is increased. We observe that $\bar{\mathcal{F}}$ is close to 1 for a broad range of parameters, highlighting a large flexibility in the operational window of the FQP. Especially keeping $1 < \rho < 1.6$ allows for very flexible transfer rates. This observation aligns with Fig. 3(b), where we show the decrease of gap size for even larger hopping ratios. We note that, while the weighted fidelity $\bar{\mathcal{F}}$ signals edge-localization of the final state, it does not, however, tell how good the localization is. We therefore also compute the inverse participation ratio (IPR) to capture edge-localization properties of the pumped state; see Appendix D. The robust and on-demand dynamic transfer of the winding state by switching only two hoppings in the whole system for a wide range of parameters is one of the main findings in this work.

We also showcase results for a two-step protocol. In this two-step protocol, instead of changing both hoppings in a unit cell of C_8 simultaneously, we change them adiabatically in two separate steps, first J_1 and then J'_{N_B} see Eqs. (A3) in Appendix A 1 and also Appendix E. We compare $\bar{\mathcal{F}}$ for the one- and two-step protocols in Fig. 4(b) as a function of ρ. As clearly seen, $\bar{\mathcal{F}}$ remains close to 1 over a larger range of ρ values for the two-step protocol. The two-step protocol also supports more rapid change of parameters (higher rate Ω) than the one-step protocol. We attribute this improvement to the increase and nature of the excitation gap separating the winding state from excited states; see Appendix E. Thus, the two-step protocol enhances the FQP flexibility by adapting the transfer process.

The pumping of winding states in the FQP demonstrates that it is possible to fully transfer states from one end of the system to the other by only minimally changing parameters by leveraging the unique quasiperiodic properties of the FC. This makes our FQP prescription highly suitable for experimental realization, as it requires significantly less tuning compared to conventionally studied (periodic) SSH model-based pumps [25,28–38,40–49] or previous FC protocols [22,24,71]. Furthermore, we next demonstrate how the FQP can be used as a quantum bus between two distant qubits. Moreover, in Appendix F, we discuss a different type of FC, where the on-site chemical potentials instead belong to a Fibonacci sequence, while bond strengths remain constant throughout the chain, and replicate our results.

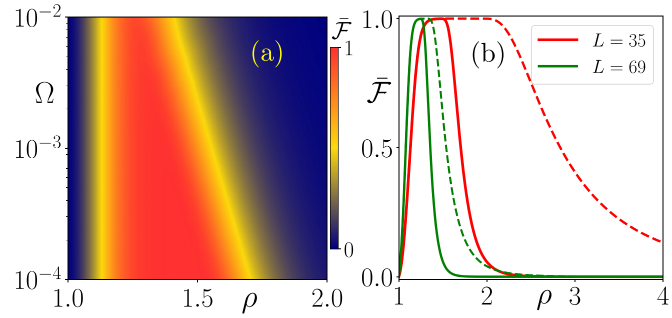

FIG. 4. (a) Weighted fidelity $\bar{\mathcal{F}}$ as a function of hopping ratio ρ and rate Ω for the C_8 FC with $L = F_8 + 1 = 35$. The frequency axis is on a logarithmic scale. (b) $\bar{\mathcal{F}}$ as a function of ρ for fixed $\Omega = 10^{-4}$ for FCs with $L = F_8 + 1 = 35$ (red) and $2F_8 + 1 = 69$ (green) for the one- (solid) and two-step (dashed) transfer protocols.

IV. STATE TRANSFER AND MAXIMAL ENTANGLEMENT BETWEEN DISTANT QUBITS

Next, we demonstrate the potential of the FQP for quantum information science. Specifically, we aim to employ the FQP as a quantum bus to control and mediate quantum information and entanglement between distant qubits, thereby enabling general-purpose quantum information processing. To this end, we couple the FQP to two outer qubits, Q_1 and Q_2, with a coupling strength g, as schematically illustrated in Fig. 1. Although the full Hamiltonian of the system in the many-body basis is considerably large, the problem can be effectively simplified by assuming that the outer qubits interact only with the winding state. Such an approximation has previously successfully been employed for matching energies between a qubit and the outer state [76]. We therefore approximate the full system with an effective three-site Hamiltonian, $\tilde{H}_{\rm MB}(t)$; see Eq. (A7) in Appendix A 4. Employing $\tilde{H}_{\rm MB}(t)$ and only considering the even occupation sector (see Appendix A 4), we obtain the time-evolved state: $\tilde{\Psi}_{\rm MB}(t) = \alpha_1(t)\,|110\rangle + \alpha_2(t)\,|101\rangle + \alpha_3(t)\,|011\rangle$, where we employ the basis states $|n_l n_r n_w\rangle$ with n_l, n_r, and n_w representing the occupation of the left and right qubits, and the winding state, respectively, taking values 0, 1. Hence, the time-dependent weights $\alpha_{1,2,3}(t)$, carry all the quantum information stored in $\tilde{\Psi}_{\rm MB}(t)$. For instance, the concurrence between the two outer qubits, given by $C = 2|\alpha_2(t)\alpha_3(t)|$, quantifies their entanglement [77,78]. We further set the qubit internal energies to $E_l = E_r = 0$ and the coupling strength between qubits and the FQP to $g = 0.1$, but we verify that our results do not depend on this specific choice.

We employ the FQP to both transfer information between the qubits and generate entanglement. We start by showing the

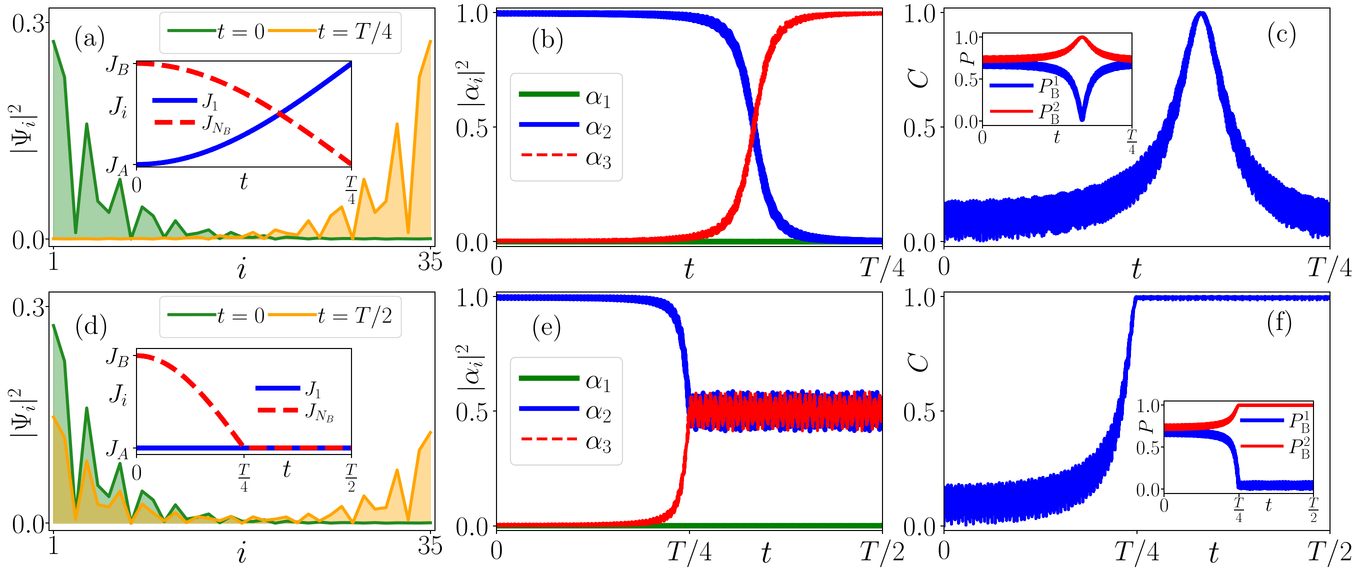

FIG. 5. (a) Spatially resolved amplitude of the winding state at initial time $t = 0$ (green) and final time $t = t_f$ (orange) using the transfer protocol in inset with changes only to the hopping amplitudes J_1 and J_{N_B}. (b) Amplitudes $|\alpha_{1,2,3}(t)|^2$ of the time-evolved many-body state for initial state $|101\rangle$ as a function of time. (c) Concurrence C as a function of time for the same initial state as in (b). Inset shows the probability of obtaining the two Bell states. (d), (e) Repeats (a)–(c) but changes only one of the hopping amplitudes in the unit cell. Here we use the C_8 FC with $L = F_8 + 1 = 35$ and $\rho = 1.4$, while $g = 1.0$, $\Omega = 10^{-4}$, and $E_l = E_r = 0.0$.

result of the time evolution of the winding state governed by the instantaneous FC Hamiltonian $H(t)$ (see Appendix A 2) in Fig. 5(a) for the one-step transfer protocol, thus reproducing Fig. 3(c) but now only focusing on the initial time ($t = 0$, green) and final time ($t = t_f$, orange). The insets show how the outermost hoppings J_1 and J_{N_B} are changing during the one-step transfer protocol. Figures 5(b) and 5(c) then illustrate how the qubits $Q_{1,2}$ are influenced by this transfer of the winding state between the two ends of the FQP, when the system is initially prepared in the unentangled state $|101\rangle$. Thus, at $t = 0$, the left (right) qubit is occupied (unoccupied), with the transferring state (winding state) also occupied. Specifically, in Fig. 5(b) we plot the amplitudes of the weights $|\alpha_{1,2,3}(t)|^2$ of the time-evolved state $\tilde{\Psi}_{\rm MB}(t)$. We observe that $|\alpha_2(t)|^2$ ($|\alpha_3(t)|^2$) evolve from one (zero) at the initial time $t_0 = 0$ to zero (one) at the final time $t_f = T/4$, while $|\alpha_1(t)|^2 = 0$. Thus, at $t_f = T/4$, the system reaches the state $|011\rangle$, indicating that the quantum information has been fully transferred from the left qubit to the right qubit. This transfer occurs as the winding state moves from the left end to the right end of the FQP, see Fig. 5(a), demonstrating the capability of the FQP to operate as a quantum bus, enabling quantum information transfer between two spatially separated qubits.

The information transfer in Fig. 5(b) occurs via entanglement between the two qubits, mediated by the FQP. Figure 5(c) illustrates the entanglement dynamics in terms of the time-dependence of the concurrence C between the two qubits. As seen, the qubits start unentangled in $|101\rangle$, then the entanglement gradually increases as the winding state propagates across the chain. Midway through the transfer, when $J_1 < J_{N_B}$ switches to $J_1 > J_{N_B}$, the two qubits become maximally entangled, before again decreasing to the unentangled state $|011\rangle$, indicating completion of the quantum state transfer. At maximum concurrence, the time-evolved state also becomes identical to a Bell state. This is seen in the inset of Fig. 5(c), where we plot the overlap with the two Bell states, $P_{\rm B}^{1,2} = |\langle\tilde{\Psi}_{\rm MB}(t)|\Psi_{\rm B}^{1,2}\rangle|$, with the Bell states defined as $\Psi_{\rm B}^{1,2} = (|101\rangle \pm |011\rangle)/\sqrt{2}$. In Appendix G, we provide complementary results for state transfer and entanglement dynamics for different initial states.

The limited time-window for maximum entanglement in Fig. 5(c) can be improved if we stop the protocol of the FQP at the peak point of the concurrence. However, this switching point is sharp and may be difficult to control; see Appendix G. Instead, we engineer maximum entanglement by using a partial-state transfer protocol where only J_{N_B} changes from $J_B \to J_A$, while J_1 remains fixed at J_A; see inset of Fig. 5(d) and Eq. (A4) in Appendix A 1 for the explicit form of this protocol. For this protocol, we set the final time to $t_f = T/2$ to show entanglement stability, but the switching of J_{N_B} is complete already at $t = T/4$. In Fig. 5(d), we show that the initial state (green) does not get completely transferred from the left to the right end of the FC; rather, the final state (orange) is now localized at both ends of the chain in a superposition. As a consequence, the qubits become coupled via the FQP. We verify this in Fig. 5(e), again starting with the initial state $|101\rangle$ but now ending up with an equal superposition of the $|101\rangle$ and $|011\rangle$ from $t = T/4$ and onward. The result is maximal concurrence $C = 1$ and the Bell state $\Psi_{\rm B}^2$, as seen in Fig. 5(f). This demonstrates that the FQP can be used both to transfer states between qubits and to prepare maximally entangled states between them.

V. SUMMARY AND OUTLOOK

In this work, we show that the intriguing quasiperiodic properties of the FC can be successfully utilized to construct a FQP that requires modulating only two single couplings to allow for complete state transfer of a quasicrystal winding state, likely making it the minimal possible topological pump. In particular, we demonstrate complete quantum pumping of winding states from one end of the chain to the other by solving for the full time dependence and keeping adiabatic evolution. The parameter range for successful pumping with maximal fidelity is large and highly tunable by both configuring the FC chain and the transfer protocol. Importantly, we also demonstrate that the FQP acts as a quantum bus for mediating quantum information exchange between two distant qubits by being able to both perform perfect quantum state transfer between the qubits and generate a maximally entangled Bell state.

While we have demonstrated a FQP with quantum state transfer and maximal entanglement generation, we envision that more general quasicrystals may possibly have even more improved properties, for example, larger gaps protecting adiabatic evolution from excited states or stronger winding state localization. Moreover, optimization of the FQP operation also involves optimization of the transfer protocol. For example, achieving even faster transfer rates might be possible by specially engineered protocols, such as following the framework of shortcuts to adiabaticity [79,80]. Still, our one- and two-step protocols are highly beneficial and may actually be easier to implement, as we only change two couplings in a straightforward simultaneous or successive manner, resulting in very simple protocols.

Our work provides the necessary proof of principle to investigate the experimental realization in quasiperiodic systems but also paves the way for many other interesting further studies. For instance, the impact of the environment on the FQP warrants further investigation. Coupling to the environment can lead to dissipation, which may induce decoherence during the transfer protocol and modify the FQP operation regime [81,82]. In contrast, dissipation has also been exploited to induce topologically protected states [83–86] and have even been shown to improve the state transfer in some cases [87,88].

Our FQP setup is likely possible to implement in multiple different experimental setups. One of the potential platforms is a lattice of superconducting resonators [72], where modifying couplings between different resonators using an electrostatic gate potential has already been employed to engineer the SSH model. Instead, utilizing the FQP requires only one or two gate potential changes, while for the SSH model, the number of changes scales with the total length of the chain. Another potential setup may be fermionic simulators made out of arrays of coherently coupled Josephson junctions [73]. Also, photonic waveguide arrays can be employed to realize the FQP, where a hopping Hamiltonian can be engineered, with longer (shorter) separation between two waveguides effectively describing weaker (stronger) bond strengths. In this latter setup, the propagation direction of light mimics the time axis. However, unlike previous implementations [22,24], requiring changing all the interwaveguide distances along the propagation direction to pump a state, our approach simplifies the setup substantially by only requiring adjustment of the outermost waveguides, keeping all the others fixed. Thus, our work highlights the advantages of quasiperiodic systems for long-range entanglement and quantum state transfer, potentially facilitating quantum experiments and simplifying quantum algorithms.

ACKNOWLEDGMENTS

We acknowledge A. Kobiałka and V. K. Vimal for helpful discussions. We acknowledge financial support from the Swedish Research Council (Vetenskapsrådet) Grant No. 2022-03963 and the European Research Council (ERC) under the European Union's Horizon 2020 research and innovation program (ERC-2022-CoG, Grant Agreement No. 101087096). Part of the computations were enabled by resources provided by the National Academic Infrastructure for Supercomputing in Sweden (NAISS), partially funded by the Swedish Research Council through Grant Agreement No. 2022-06725. R.S.S. acknowledges funding from the Spanish Comunidad de Madrid (CM) Talento Program (Project No. 2022-T1/IND- 24070), and the Spanish Ministry of Science, innovation, and Universities through Grant No. PID2022-140552NA-I00.

DATA AVAILABILITY

The data that support the findings of this article are openly available [89].

APPENDIX A: METHODS

1. Transfer protocols

To transfer a state between the two ends of the FC, we dynamically change the hopping parameters. In Figs. 3(a)–3(c), and 5(a)–5(c), we employ the one-step protocol. Explicitly, the one-step protocol reads

$$V(t) = \left\{J_i^{\phi_1}\right\} + \left(\left\{J_i^{\phi_2}\right\} - \left\{J_i^{\phi_1}\right\}\right)(1 - \cos\Omega t),\ t \in [0, T/4], \tag{A1}$$

where $\{J_i^{\phi_{1,2}}\}$ represents the hopping sequence corresponding to phason angles $\phi_{1,2}$, while Ω is the transfer rate. Further, $T = 2\pi/\Omega$ and we set $t_f = T/4$ to the time where the process is completed. Note that the transfer protocol $V(t)$ only changes the two outermost hoppings in the FC (or two hoppings per approximant repetition), see Fig. 2(b), while all other hoppings remain unchanged. Explicitly, the two outermost hoppings change as

$$\begin{aligned} J_1(t) &= J_B - (J_B - J_A)\cos\Omega t, \quad t \in [0, T/4],\\ J_{N_B}(t) &= J_A + (J_B - J_A)\cos\Omega t, \quad t \in [0, T/4], \end{aligned} \tag{A2}$$

illustrated in the inset of Fig. 5(a). In FCs repeating a single approximant l times, e.g., in Figs. 3(a) and 4(b), we repeat Eqs. (A2) in each approximant, resulting in $2l$ hoppings being changed. We illustrate such a change of multiple hoppings for a repeated chain in Fig. 6.

The two-step protocol we employ in Fig. 4(b) instead explicitly reads as

$$\begin{aligned} J_1(t) &= J_B - (J_B - J_A)\cos\Omega t, \quad t \in [0, T/4],\\ J_{N_B}(t) &= J_B + (J_B - J_A)\cos\Omega t, \quad t \in [T/4, T/2]. \end{aligned} \tag{A3}$$

For this two-step protocol, we instead set $t_f = T/2$ to the time where the process is completed. The hopping changes in the two-step protocol are shown in Fig. 10 in Appendix E.

Finally, to generate entanglement in Figs. 5(d) and 5(e), we use the partial-transfer protocol where we only change one of the hoppings as

$$J_{N_B}(t) = J_A + (J_B - J_A)\cos\Omega t, \quad t \in [0, T/4], \tag{A4}$$

while J_1 remains fixed at J_A. For this protocol, the hopping change is completed at $t = T/4$, but in Figs. 5(d) and 5(e), we still study the system until $t = T/2$ to show that we retain maximal entanglement.

2. Time evolution

For the one-step transfer protocol, we obtain the instantaneous Hamiltonian $H(t)$ at time t by using the hopping sequence $V(t)$ in Eq. (A1), such that $H(t) = H[V(t)]$, with $H(0) = H[\{J_i^{\phi_1}\}]$. To obtain time-evolved states, we construct the time-evolution operator in a time-ordered ($\mathcal{T}$) manner as $U(t,0) = \mathcal{T}\exp[-i\int_0^t H(t')dt']$. We then compute the time-evolved state $\psi(t)$ as $\psi(t) = U(t,0)\psi_w(0)$, where $\psi_w(0)$ represents the winding state of the Hamiltonian $H(0)$ at initial time $t = 0$, corresponding to the hopping sequence for the phason angle ϕ_1. Then at final time $t_f = T/4$, the Hamiltonian $H(t_f)$ represents a FC with a hopping sequence generated for the phason angle ϕ_2, where $T = 2\pi/\Omega$ with transfer rate Ω. Similarly, for the two-step and partial-transfer protocols, we use Eqs. (A3) and (A4), respectively, to obtain $H(t)$ and thereby their time-evolution operators $U(t,0)$.

3. Fidelity

We define a weighted fidelity $\bar{\mathcal{F}}$ employing the target state $\psi_{\rm T}$ as

$$\bar{\mathcal{F}} = \alpha|\langle\psi(t = t_f)|\psi_{\rm T}\rangle|^2, \tag{A5}$$

where $\psi_{\rm T}$ is the winding state of the FC Hamiltonian for ϕ_2: $\psi_{\rm T} = \psi_w^{\phi_2}$; see orange state in Fig. 2(c). Here, $\psi(t = t_f)$ is the time-evolved winding state, while the weight α is computed as $\alpha = (|\psi_{L,\rm T}|^2 - |\psi_{1,\rm T}|^2)/\text{maximum}(\{|\psi_{i,\rm T}|^2\})$; with $\psi_{i,\rm T}$ being the elements of $\psi_{\rm T}$ at lattice sites i, with L the last site of the chain. Including α into a weighted fidelity ensures that the target state is an edge state with a maximum weight at the right end of the chain. We find that this is important close to $\rho \simeq 1$, where the chain starts to resemble a 1D metal with an almost delocalized winding state.

4. Effective qubit-FQP-qubit setup

We model the qubit-FQP-qubit system as an effective three-site system, with the middle site being constructed out of the time-evolved winding state $\psi(t)$ that we numerically obtain by evolving $\psi_w(0)$ using $U(t,0)$. When the energies of the qubits are close to that of the winding state $\psi(t)$, the qubits interact only with the winding state, and we can then safely work with this effective three-site Hamiltonian [76]. In practice, this means we need to numerically extract the energy of the winding state and its weight on the first site, $i = 1$, and last site, $i = L$, of the FC at each time t. These weights then determine the coupling with the corresponding qubit. In this description, the effective Hamiltonian of the system reads [76]

$$\begin{aligned}\tilde{H} = {}& E_w(t)c_w^\dagger c_w + E_l d_l^\dagger d_l + E_r d_r^\dagger d_r \\ &+ g a_l(t) d_l^\dagger c_w + g a_r(t) c_w^\dagger d_r + \text{H.c.},\end{aligned} \tag{A6}$$

where $E_w(t)$ ($c_w^\dagger$), E_l ($d_l^\dagger$), and E_w ($d_r^\dagger$) are the energies (electronic creation operators) of the time-evolved winding state, left, and right qubits, respectively. The energy $E_w(t)$ here becomes a time-dependent parameter that we obtain from the eigenvalues of $H(t)$; see, e.g., solid curves in Figs. 3(a) and 3(b). The qubit energies $E_{l,r}$ should, in principle, be chosen close to $E_w(t)$. However, once we make the approximation that the qubits are only interacting with the time-evolved winding state and construct the Hamiltonian in Eq. (A6), we find that the choices for $E_{l,r}$ do not matter as much and we therefore set them to zero for simplicity. We verify that different values of $E_{l,r}$ do not alter our discussion. Moreover, $a_l(t) = |\psi_{i=1}(t)|^2$ ($a_r(t) = |\psi_{i=L}(t)|^2$) is the weight of the time-evolved winding state at the left (right) end of the chain, which we extract numerically at each time, while g is a free parameter controlling the coupling strength between the winding state and the qubit.

To solve the Hamiltonian Eq. (A6), we consider a basis $|n_l n_r n_w\rangle$, where n_l, n_r, and n_w represent the occupation of the left qubit state, right qubit state, and the time-evolved winding state, respectively, taking values $n = 0, 1$. Since the Hamiltonian in Eq. (A6) preserves the number of particles, it does not couple even and odd number of particle sectors, and we can focus on only the even number of particles sector, while an analysis of odd number of particles sector gives the same results. We thus use the even sector basis: $(\{|101\rangle, |011\rangle, |110\rangle\}^{\tilde{T}})$; with $\tilde{T}$ representing transpose, with the many-body Hamiltonian in this basis reading as

$$\tilde{H}_{\rm MB}(t) = \begin{pmatrix} E_l + E_r & g a_r(t) & g a_l(t) \\ g a_r(t) & E_l + E_w(t) & 0 \\ g a_l(t) & 0 & E_r + E_w(t)\end{pmatrix}. \tag{A7}$$

We here omit the $|000\rangle$ state as there is no term in the Hamiltonian associated with this state. We employ the Hamiltonian in Eq. (A7) to construct the time-evolution operator $\tilde{U}_{\rm MB}(t,0) = \mathcal{T}\exp[-i\int_0^t \tilde{H}_{\rm MB}(t')dt']$ and compute the time-evolved many-body state as $\tilde{\Psi}_{\rm MB}(t) = \tilde{U}_{\rm MB}(t,0)\tilde{\Psi}_{\rm MB}(0)$. This time-evolved state can always be expressed as $\tilde{\Psi}_{\rm MB}(t) = \alpha_1(t)|110\rangle + \alpha_2(t)|101\rangle + \alpha_3(t)|011\rangle$. Thus, the time-dependent weights $\alpha_{1,2,3}(t)$ govern all properties, including the dynamics of the quantum state transfer and the qubit-qubit entanglement distribution.

APPENDIX B: FIBONACCI QUANTUM PUMP USING DIFFERENT FIBONACCI CHAINS

In the main text, we discuss the FQP, employing the C_8 FC, mainly for one repetition ($l = 1$), but also for two ($l = 2$). Here, we demonstrate that the FQP can also easily be implemented using other approximants. To this end, we first consider the C_6 and C_7 FC approximants, but we obtain analogous results also for other approximants. We then also extract the excitation gaps for the winding states for different lengths and generations of the FCs.

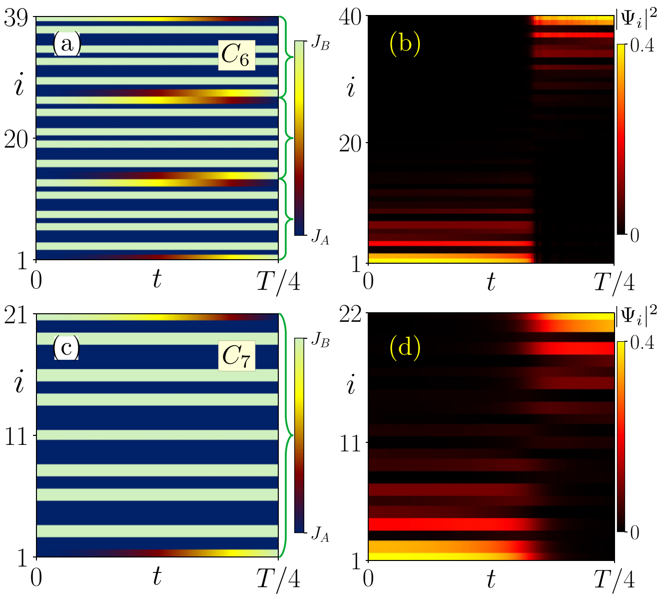

FIG. 6. (a) Dynamical change of hoppings as a function of time t for the C_6 FC with $l = 3$ repetitions such that $L = 3F_6 + 1 = 40$, with colors representing the amplitude of the hopping, with J_A (blue) and J_B (green). Curly brackets represent one unit cell of the FC. (b) Pumping of the winding state as a function of lattice site i and time t for the dynamical change of hoppings in (a). (c-d) Repeats (a-b) but for the C_7 FC with $l = 1$ such that $L = F_7 = 22$. Here $\rho = 1.5$, $\Omega = 10^{-4}$.

The unit cell of C_6 FC consists of 13 bonds ($N_B = 13$). In Figs. 6(a) and 6(b), we demonstrate the same transfer protocol as in Eq. (A1) but employing a chain comprising of three repetitions ($l = 3$) of the C_6 FC, such that the number of sites is $L = 3F_6 + 1 = 40$. This means that we change the two outer bonds in each unit cell, i.e., J_1 and J_{N_B}, of the C_6 FC dynamically, resulting in a total of six bonds being changed. We explicitly showcase this dynamic change of the bonds in Fig. 6(a), where the unit cell is indicated by curly brackets. In Fig. 6(b), we then show how this results in a complete pumping of the winding state from one end to the other of the FC. In Figs. 6(c) and 6(d), we similarly demonstrate the FQP for a C_7 FC with only one repetition such that $L = 21 + 1 = 22$. We again dynamically change only the two outermost hoppings, with the change in hoppings as a function of time t shown in Fig. 6(c), while Fig. 6(d) shows the pumping of the winding state. Note that, in this case, we only need to change two of the hoppings.

The results in the main text and here in Fig. 6 illustrate some trade-offs for the choice of FC for the FQP. Using a higher generation of the FC can be beneficial, as then we can reach a longer chain, or transfer distance, with fewer hoppings that need to be changed. For instance, a single unit cell ($l = 1$) only requires changing the two outermost hoppings, making it likely a minimal topological quantum pump. In contrast, shorter approximants of the FC require us to make two changes per unit cell (l). Still, repeating unit cells might be desirable in order to create a more localized winding state. This is seen in Fig. 6, where the winding state in Fig. 6(d) is notably less localized than in Fig. 6(b).

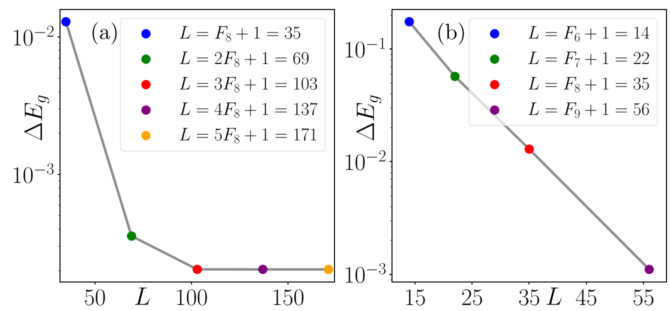

FIG. 7. (a) Excitation gap ΔE_g as a function of system sizes L for multiple repetitions l of the C_8 FC. (b) Excitation gap ΔE_g gap for a single unit cell $l = 1$ of different FC approximants. Here we use $\mu = 0$ and $\rho = 1.5$.

On the other hand, while longer FCs have a more strongly localized winding state, the excitation gap, ΔE_g, that separates the winding state from the next excited state during time evolution decreases with the increase in system size. We demonstrate this feature in Fig. 7. In particular, Fig. 7(a) shows the excitation gap ΔE_g for different system sizes L for the FC approximant C_8. We observe that the excitation gap notably decreases with system size. This figure complements Fig. 3(a) in the main text. In Fig. 7(b), we additionally illustrate the excitation gap ΔE_g for a single unit cell ($l = 1$) of different Fibonacci approximants. For longer approximants, we again have a longer chain, and the excitation gap decreases. Thus, for longer FC chains, we need to have a smaller rate that changes the bonds more slowly to be able to adiabatically pump the winding state. Depending on the demands for speed, localization, fidelity, and simplicity of implementation, different FCs might thus best fulfill the desired requirements.

APPENDIX C: ROBUSTNESS AGAINST DISORDER

In the main text, we discuss the phase diagram for successful state transfer in Fig. 4 in terms of the weighted fidelity $\bar{\mathcal{F}}$. However, we there do not consider any disorder. Here, we study the effect of disorder on the operation of the FQP.

We again focus on the C_8 FC, as in the main text, but now also add disorder in either the on-site ($\mu + W_i$) or hopping ($J_i + W_i$) terms in the Hamiltonian in Eq. (1) in the main text. Here, W_i represents disorder, which we assume to be uniformly distributed using $W_i \in [-u/2, u/2]$, with u representing the disorder strength in units of J_A. We focus on the weighted fidelity $\bar{\mathcal{F}}$, an observable that quantifies successful FQP operation. We compute the weighted fidelity $\bar{\mathcal{F}}$ for different random disorder configurations and then take an average over 50 disorder configurations for each u.

In Fig. 8, we plot the disorder-averaged weighted fidelity $\langle\bar{\mathcal{F}}\rangle$ as a function of the disorder strength u for on-site (a) and hopping (b) disorder, respectively. We find that the weighted fidelity $\langle\bar{\mathcal{F}}\rangle$ remains close to 1 for small to moderate disorder strengths, but eventually diminishes as we increase the disorder strength. For hopping disorder, the fidelity decreases somewhat faster, which we attribute to it breaking quasiperiodicity. Nevertheless, these results show that the FQP displays remarkable robustness against disorder.

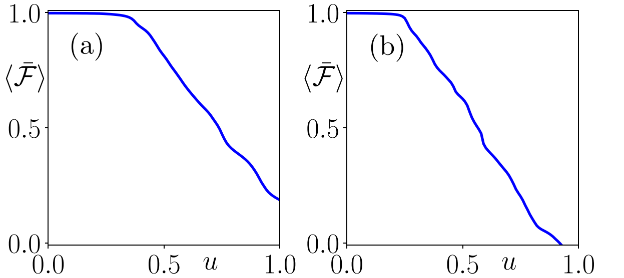

FIG. 8. Disorder-averaged weighted fidelity $\langle\bar{\mathcal{F}}\rangle$ as a function of the disorder strength u for (a) on-site and (b) hopping disorder. Here we use the C_8 FC with $L = F_8 + 1 = 35$, $\mu = 0$, $\rho = 1.4$, and $\Omega = 10^{-4}$ and average over 50 random disorder configurations for each u.

APPENDIX D: LOCALIZATION PROPERTIES

In Fig. 4(a), we study the phase diagram for the one-step protocol in terms of the weighted fidelity. By choosing to study a weighted fidelity, expressed in Eq. (A5), we know that the final state is mainly located at the right end of the chain, but it does not give us any information about the degree of localization. Here, we provide additional information about the localization properties by studying the IPR.

The IPR for the time-evolved winding state is defined as $\mathrm{IPR} = |\psi(t = t_f)|^4$. A (lower) higher value of IPR thus indicates a (de)localized state. We plot the IPR as a function of the hopping ratio ρ and the rate Ω in Fig. 9(a), i.e., analogous to the phase diagram for the weighted fidelity in Fig. 4(a) in the main text. Our results illustrate that if a sharply localized state is desired, we may resort to a higher value of hopping ratio ρ, but in that case, the parameter change rate should be a bit slower. In Fig. 9(b), we also repeat Fig. 4(b) in the main text, but for the IPR, by comparing the IPR for one-step (solid) and two-step (dashed) protocols for different system sizes $L = F_8 + 1 = 35$ (red) and $2F_8 + 1 = 69$ (green) as a function of the hopping ratio ρ. As we increase the chain length, we find a smaller range with higher IPR, while for the two-step protocol, the range for a higher IPR is larger compared to the one-step protocol, both resulting in overall agreement with the behavior of the weighted fidelity. Thus, these results show that the IPR and the weighted fidelity largely track each other and that it is possible to design the FC and the transfer protocol to reach a high weighted fidelity and IPR.

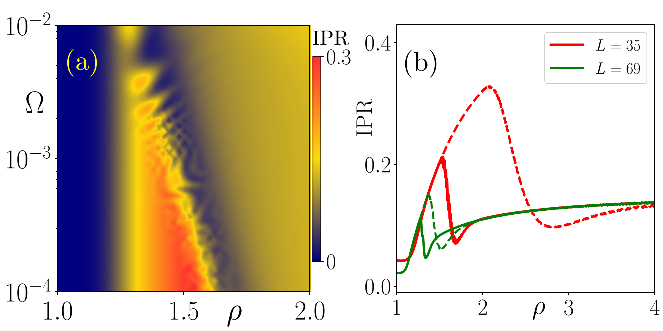

FIG. 9. (a) IPR as a function of hopping ratio ρ and rate Ω for C_8 FC with $L = F_8 + 1 = 35$ using the one-step protocol. The frequency axis is on a logarithmic scale. (b) IPR as a function of ρ for a fixed $\Omega = 10^{-4}$ for FCs with $L = F_8 + 1 = 35$ (red) and $L = 2F_8 + 1 = 69$ (green) for the one- (solid) and two-step (dashed) transfer protocols. Same systems and plots as Fig. 4 in the main text but for the IPR instead of the weighted fidelity.

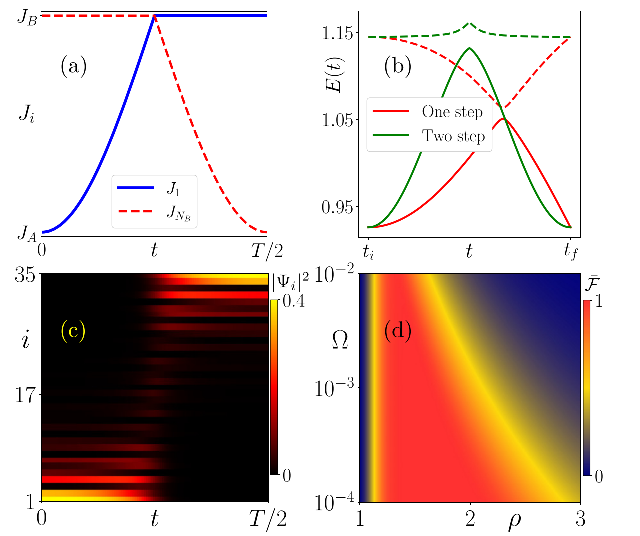

FIG. 10. (a) Dynamic change of hoppings J_1 and J_{N_B} inside the unit cell of C_8 FC as a function of time in the two-step protocol, Eqs. (E1). (b) Comparison of the excitation gap between the winding state and the next excited state in the one-step, Eqs. (A2) (red) and two-step, Eqs. (E1) (green) protocols. (c) Pumping of the winding state for the two-step protocol. (d) Weighted fidelity $\bar{\mathcal{F}}$ as a function of hopping ratio ρ and rate Ω in the two-step protocol. The frequency axis is on a logarithmic scale. Here, $L = F_8 + 1 = 35$, $\rho = 1.5$ and $\Omega = 10^{-4}$ for (a)–(c).

APPENDIX E: TWO-STEP PROTOCOL

In the main text, we discuss some of the results of a two-step transfer protocol. In particular, as shown in Fig. 4(b) in the main text, the two-step protocol has an advantage of a larger region of high fidelity compared to the one-step protocol given by Eqs. (A1) and (A2). Here, we discuss the details of the two-step protocol and some results associated with it.

In terms of the change in the outermost hoppings J_1 and J_{N_B}, the two-step protocol reads

$$\begin{aligned} J_1(t) &= J_B - (J_B - J_A)\cos\Omega t, \quad t \in [0, T/4], \\ J_{N_B}(t) &= J_B + (J_B - J_A)\cos\Omega t, \quad t \in [T/4, T/2]. \end{aligned} \tag{E1}$$

In Fig. 10(a), we plot the time dependence of these two hoppings, with the hopping J_1 (blue) first switched from J_A to J_B, and only once that is completed we start switching the other hopping J_{N_B} (red) from J_B to J_A, to be compared to the one-step protocol illustrated in the inset of Fig. 5(a) in the main text. In Fig. 10(b), we then plot the evolution of the eigenvalues of the winding state (solid) and the next excited state (dashed) for one-step (red) and two-step (green) protocols. Since the final times for the one- and two-step protocols are different, we here, for plotting purposes, scale them such that t_f is the same for both protocols. We find that the excitation gap isolating the winding state from the next excited state for the two-step protocol is slightly larger compared to the one-step protocol. Although this difference is small, it has a notable effect on the FQP operations as explained below. We also note that at the minimum gap, the evolution of the winding state and the excited state display a clear kink. This kink appears at the time instance when we interchange which hopping is being changed. We can therefore attribute the kinklike feature in the excitation gap to the fact that the changes in the hoppings also display kinks.

In Fig. 10(c), we show the pumping of the winding state employing the two-step protocol. In comparison to the one-step protocol, see Fig. 3(c) in the main text, the transition period when the winding state lives on both ends of the system is longer. In Fig. 10(d), we depict the phase diagram in terms of the weighted fidelity $\bar{\mathcal{F}}$ (colorbar) as a function of the hopping ratio ρ and rate Ω for the two-step protocol. The region with $\bar{\mathcal{F}} \simeq 1$ is more extended for the two-step protocol compared to the one-step protocol displayed in Fig. 4(a) in the main text. Thus, these results supplement the results shown in Figs. 3 and 4 in the main text and demonstrate how a different transfer protocol can lead to a wider region of parameters for successful FQP operation.

APPENDIX F: ONSITE FIBONACCI CHAIN

In the main text, we discuss results based on a hopping FC model. However, we can also build an FC employing an on-site FC model. Here, show that a FQP can also be constructed using winding states of an on-site FC.

In the on-site FC, the on-site chemical potential μ_i varies according to the Fibonacci sequence, while the hopping J remains constant. We can write the Hamiltonian for an on-site FC as [61]

$$H = \sum_i \mu_i c_i^\dagger c_i + J \sum_i c_i^\dagger c_{i+1} + \text{H.c.}, \tag{F1}$$

where the site-dependent μ_i take values as low (μ_A) and high (μ_B) chemical potentials, with $\{\mu_i\}$ belonging to the nth Fibonacci approximant $\{C_n\}$, such that $C_0 = \mu_B$, $C_1 = \mu_A$, $C_2 = \mu_A\mu_B$, $C_3 = \mu_A\mu_B\mu_A$, $C_4 = \mu_A\mu_B\mu_A\mu_A\mu_B$, and so on [61]. Thus, the total number of sites in C_n equals the Fibonacci number $F_n = F_{n-1} + F_{n-2}\ \forall n \geqslant 2$, with $F_0 = 1$, $F_1 = 1$. Note that the number of bonds in a unit cell is $N_B = F_n - 1$ here, while the hopping model has $N_B = F_n$ number of bonds. Similar to the FC hopping model, we can construct longer on-site FCs by either considering larger approximants C_n, or repeating the approximant C_n l times, such that the total number of lattice sites of the chain is given as $L = lF_n$. We also again employ OBCs and consider a dimensionless parameter $\tilde{\rho} = \mu_B/\mu_A$, while setting $\mu_A = J = 1$ throughout this appendix and expressing all variables with the dimensions of energy in units of the hopping amplitude J.

We consider the C_8 FC with $L = F_8 = 34$ lattice sites and demonstrate the eigenvalue spectra as a function of the phason angle ϕ in Fig. 11(a). The red energy in Fig. 11(a) marks a winding states inside a quasicrystal gap shaded by gray. In this quasicrystal gap, the winding state winds once, and the gap has gap label $\mathcal{C} = 1$. Next, we focus on two specific values of the phason angle ϕ_1 and ϕ_2, denoted by the dashed green and orange lines in Fig. 11(a). We choose these $\phi_{1,2}$ such that the change of the phason angle from ϕ_1 to ϕ_2 amounts to only

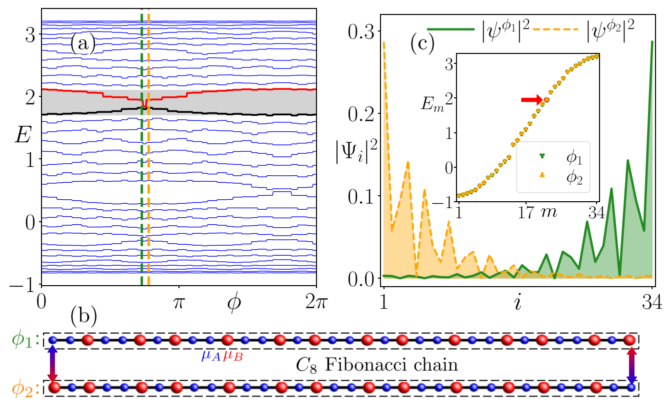

FIG. 11. (a) Eigenvalues E as a function of phason angle ϕ. Red curve represents a winding state in one of the quasicrystal gaps (gray shaded). (b) Flipping between high (red) and low (blue) on-site chemical potentials, indicated by the arrows when changing phason angles from ϕ_1 (green) to ϕ_2 (orange), also marked in (a). (c) Eigenstate of the winding state (red) along the chain at ϕ_1 (green) and ϕ_2 (orange). Inset shows eigenvalue spectrum E_m as a function of the state index m for phason angles ϕ_1 (green) and ϕ_2 (orange), with red dot marking the winding state. Here we use the C_8 FC with $L = F_8 = 34$ sites and $\tilde{\rho} = 1.5$, $\phi_1 = 0.73\pi$, and $\phi_2 = 0.78\pi$.

flipping the two outermost chemical potentials in a unit cell of the C_8 FC, as denoted by the arrows in Fig. 11(b). This is analogous to the setup in Fig. 2(b) in the main text. We denote these two chemical potentials as μ_1 and μ_{N_B+1}. We plot the eigenvalue spectrum for ϕ_1 (green) and ϕ_2 (orange) in the inset of Fig. 11(c) and see that they perfectly overlap, with with winding state marked in red appearing around $E_m \simeq 2.0$. Then, in Fig. 11(c), we investigate the spatial extent of the winding state for the phason angles ϕ_1 (green) and ϕ_2 (orange) and find that it completely switches between the two ends of the chain with the change of phason angle. These results are thus analogous to Fig. 2 in the main text and demonstrate that winding states in the on-site FC can also be employed for FQP operation.

For completeness, we explicitly demonstrate FQP operations for the on-site FC. We consider a similar one-step transfer protocol as for the hopping FC model in the main

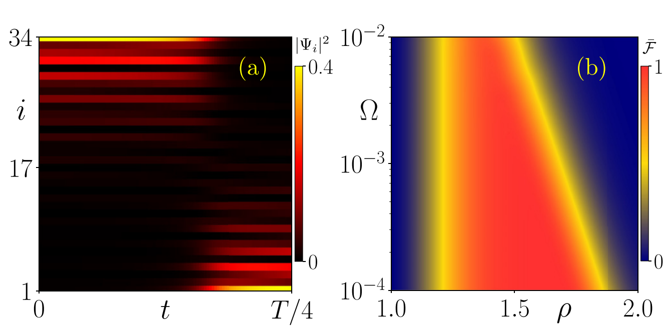

FIG. 12. (a) Evolution of the winding state as a function of time t and spatial position i for the C_8 FC in Fig. 11. Here $\Omega = 10^{-4}$ and $\rho = 1.5$. (b) Weighted fidelity $\bar{\mathcal{F}}$ as a function of hopping ratio $\tilde{\rho}$ and rate Ω. The frequency axis is on a logarithmic scale.

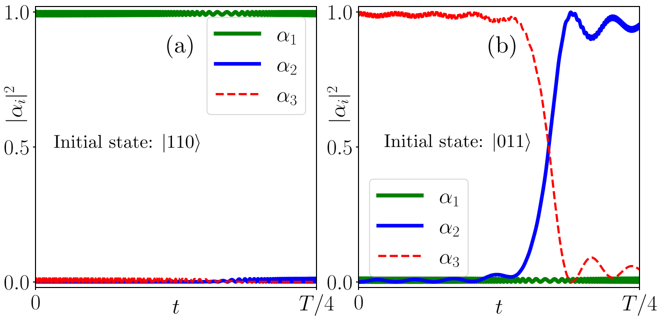

FIG. 13. (a) Amplitudes $|\alpha_{1,2,3}(t)|^2$ of the time-evolved many-body state for an initial state (a) $|110\rangle$ and (b) $|011\rangle$ as a function of time. The figures reproduce Fig. 5(b) from the main text but with other initial states, while all other parameters are the same, except $g = 0.1$ to reduce the oscillation of the time-evolved state.

text, i.e. Eq. (A1). The transfer protocol thus reads

$$V(t) = \{\mu_i^{\phi_1}\} + (\{\mu_i^{\phi_2}\} - \{\mu_i^{\phi_1}\})(1 - \cos \Omega t),\quad t \in [0, T/4], \tag{F2}$$

where $\{\mu_i^{\phi_i}\}$ represents the chemical potential sequence corresponding to phason angle ϕ_i and Ω indicates the rate. Note that there is only a change of two chemical potentials in a unit cell in $V(t)$ as shown in Fig. 11(b), while others remain the same, similar to the hopping FC transfer protocol employed in the main text. More explicitly, in terms of the chemical potential μ_{1,N_B+1}, the transfer protocol reads

$$\begin{aligned} \mu_1(t) =& \mu_B - (\mu_B - \mu_A)\cos \Omega t, \quad t \in [0, T/4], \\ \mu_{N_B+1}(t) =& \mu_A + (\mu_B - \mu_A)\cos \Omega t, \quad t \in [0, T/4]. \end{aligned} \tag{F3}$$

Using the one-step transfer protocol and solving for the full time-dependence as outlined in Appendix A, we demonstrate the pumping in the on-site FQP. In the main text, we show pumping of a state from left to right. Here, we display an opposite case, where we transfer a state from the right end to the left. We depict the time-resolved state transfer in Fig. 12(a), showing a winding state which is initially localized at the right end of the system being transferred to the other left end. We also compute the weighted fidelity $\bar{\mathcal{F}}$ and plot it as a function of $\tilde{\rho}$ and Ω in Fig. 12(b), thus showing complementary information to Fig. 4(a) in the main text. These results demonstrate that we can equally well use an on-site FC to perform quantum state transfer using the winding state.

APPENDIX G: STATE TRANSFER AND ENTANGLEMENT GENERATION

In the main text, we discuss state switching and entanglement generation employing the FQP and using the initial state $|101\rangle$ and the one-step protocol. Here, we provide complementary results using other initial states and protocols. First, we discuss results for different initial states. In Figs. 13(a) and 13(b), we show the coefficients $|\alpha_{1,2,3}(t)|^2$ of the time-evolved state for the initial many-body states $|110\rangle$ and $|011\rangle$, respectively. For the initial state $|110\rangle$, we do not observe any change in the time-evolved state. This is expected as both qubits are occupied initially, so there is no change in the qubit state from FQP operations. However, for the initial state $|011\rangle$, we see an analogous behavior to the state $|101\rangle$ in Fig. 5(b) in the main text.

In the main text, we discuss how the two-step protocol can be employed to expand the parameter space for high fidelity of the FQP. Here, we complement the results also for coupling the FQP to the two qubits. In particular, we demonstrate state transfer operation between two qubits when employing the two-step protocol in Fig. 14. We first show the transfer of the winding state in the FQP in Fig. 14(a). In Fig. 14(b), we then show how the coefficients $|\alpha_{1,2,3}(t)|^2$ of the time-evolved many-body state behave for an initial state $|101\rangle$ when transferring the winding state. As expected, we observe a similar behavior to Fig. 5(b) in the main text, with the qubit states getting flipped as we complete the transfer protocol. This behavior is reflected in the concurrence as well as in Fig. 14(c). The concurrence exhibits a value close to 1 when the qubit states are being flipped but we do not retain a high concurrence at the end of the transfer protocol. This behavior is also observed when we plot the overlap of the time-evolved state with the Bell states ($P_{\mathrm{B}}^{1,2}$) in the inset of Fig. 14(c). We obtain the Bell state for a short instance of time when the concurrence is 1. Thus, we observe a fully analogous scenario for the two-step protocol as that of the one-step protocol in Fig. 5(c) in the main text.

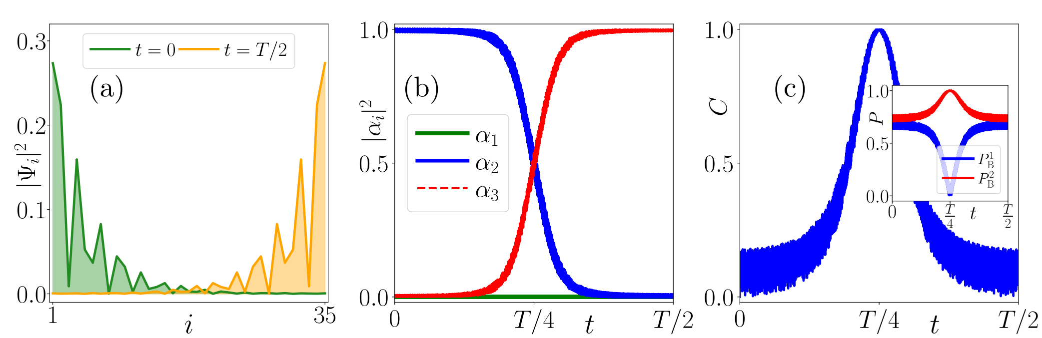

FIG. 14. (a) Spatially resolved amplitude of the winding state at initial time $t = 0$ (green) and final time $t = t_f$ (orange) using the two-step transfer protocol in Fig. 10. (b) Amplitudes $|\alpha_{1,2,3}(t)|^2$ of the time-evolved many-body state for an initial state $|101\rangle$ as a function of time. (c) Concurrence C as a function of time for the same initial state as in (b). Inset shows the probability of obtaining the two Bell states. The figures reproduce Figs. 5(a)–5(c) from the main text but with the two-step protocol, while all other parameters are the same.

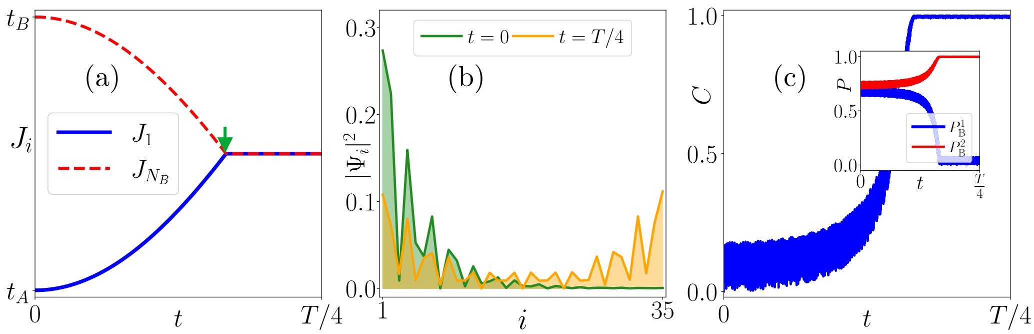

FIG. 15. (a) Modified one-step transfer protocol as a function of time t, with green arrow marking the point when we turn off the protocol. (b) Spatially resolved amplitude of the winding state at initial time $t = 0$ (green) and final time $t = t_f$ (orange) using the transfer protocol in (a). (c) Concurrence C for the initial state $|101\rangle$ as a function of time. Inset shows the probabilities of obtaining the two Bell states. The figure reproduces Figs. 5(a) and 5(c) from the main text but with the turned off one-step protocol in (a), while all other parameters are the same.

Finally, in the main text in Fig. 5(c), we observe near max $C \simeq 1$ when the winding state is switched from one side to the other of the system. However, we can then not retain this high concurrence C at the final time. Here, we show that by simply turning off the one-step protocol, we can also maintain the high concurrence at the final time t_f. Thus, we stop the change of the hoppings at the point marked by the green arrow in Fig. 15(a). When we stop our parameter-changing protocol at this point, the winding state does not get completely transferred to the other end of the system, rather, it is now localized at both ends of the chain in a superposition state, as shown in Fig. 15(b). At the same time, by stopping the transfer protocol here, we retain the maximum $C \simeq 1$ until the final time, as shown in Fig. 15(c). We also show the overlap of the time-evolved state with the Bell state in the inset of Fig. 15(c), observing that we obtain one of the Bell states.

[1] L. Trifunovic, F. L. Pedrocchi, and D. Loss, Long-distance entanglement of spin qubits via ferromagnet, Phys. Rev. X **3**, 041023 (2013).

[2] N. Roch, M. E. Schwartz, F. Motzoi, C. Macklin, R. Vijay, A. W. Eddins, A. N. Korotkov, K. B. Whaley, M. Sarovar, and I. Siddiqi, Observation of measurement-induced entanglement and quantum trajectories of remote superconducting qubits, Phys. Rev. Lett. **112**, 170501 (2014).

[3] C. H. Bennett and D. P. DiVincenzo, Quantum information and computation, Nature (London) **404**, 247 (2000).

[4] L.-M. Duan, M. D. Lukin, J. I. Cirac, and P. Zoller, Long-distance quantum communication with atomic ensembles and linear optics, Nature (London) **414**, 413 (2001).

[5] N. Gisin and R. Thew, Quantum communication, Nat. Photonics **1**, 165 (2007).

[6] T. E. Northup and R. Blatt, Quantum information transfer using photons, Nat. Photonics **8**, 356 (2014).

[7] F. Xu, X. Ma, Q. Zhang, H.-K. Lo, and J.-W. Pan, Secure quantum key distribution with realistic devices, Rev. Mod. Phys. **92**, 025002 (2020).

[8] X.-M. Hu, Y. Guo, B.-H. Liu, C.-F. Li, and G.-C. Guo, Progress in quantum teleportation, Nat. Rev. Phys. **5**, 339 (2023).

[9] H. J. Kimble, The quantum internet, Nature (London) **453**, 1023 (2008).

[10] S. Wehner, D. Elkouss, and R. Hanson, Quantum internet: A vision for the road ahead, Science **362**, eaam9288 (2018).

[11] K. Azuma, S. E. Economou, D. Elkouss, P. Hilaire, L. Jiang, H.-K. Lo, and I. Tzitrin, Quantum repeaters: From quantum networks to the quantum internet, Rev. Mod. Phys. **95**, 045006 (2023).

[12] J. I. Cirac, P. Zoller, H. J. Kimble, and H. Mabuchi, Quantum state transfer and entanglement distribution among distant nodes in a quantum network, Phys. Rev. Lett. **78**, 3221 (1997).

[13] D. N. Matsukevich and A. Kuzmich, Quantum state transfer between matter and light, Science **306**, 663 (2004).

[14] S. Bose, Quantum communication through an unmodulated spin chain, Phys. Rev. Lett. **91**, 207901 (2003).

[15] M. Christandl, N. Datta, A. Ekert, and A. J. Landahl, Perfect state transfer in quantum spin networks, Phys. Rev. Lett. **92**, 187902 (2004).

[16] N. Y. Yao, L. Jiang, A. V. Gorshkov, Z.-X. Gong, A. Zhai, L.-M. Duan, and M. D. Lukin, Robust quantum state transfer in random unpolarized spin chains, Phys. Rev. Lett. **106**, 040505 (2011).

[17] B. Vermersch, P.-O. Guimond, H. Pichler, and P. Zoller, Quantum state transfer via noisy photonic and phononic waveguides, Phys. Rev. Lett. **118**, 133601 (2017).

[18] M. Z. Hasan and C. L. Kane, *Colloquium*: Topological insulators, Rev. Mod. Phys. **82**, 3045 (2010).

[19] X.-L. Qi and S.-C. Zhang, Topological insulators and superconductors, Rev. Mod. Phys. **83**, 1057 (2011).

[20] B. A. Bernevig, *Topological Insulators and Topological Superconductors* (Princeton University Press, Princeton, 2013).

[21] R. Citro and M. Aidelsburger, Thouless pumping and topology, Nat. Rev. Phys. **5**, 87 (2023).

[22] Y. E. Kraus, Y. Lahini, Z. Ringel, M. Verbin, and O. Zilberberg, Topological states and adiabatic pumping in quasicrystals, Phys. Rev. Lett. **109**, 106402 (2012).

[23] N. Y. Yao, C. R. Laumann, A. V. Gorshkov, H. Weimer, L. Jiang, J. I. Cirac, P. Zoller, and M. D. Lukin, Topologically

protected quantum state transfer in a chiral spin liquid, Nat. Commun. **4**, 1585 (2013).
[24] M. Verbin, O. Zilberberg, Y. Lahini, Y. E. Kraus, and Y. Silberberg, Topological pumping over a photonic Fibonacci quasicrystal, Phys. Rev. B **91**, 064201 (2015).
[25] N. Lang and H. P. Büchler, Topological networks for quantum communication between distant qubits, npj Quantum Inf **3**, 47 (2017).
[26] C. Dlaska, B. Vermersch, and P. Zoller, Robust quantum state transfer via topologically protected edge channels in dipolar arrays, Quantum Sci. Technol. **2**, 015001 (2017).
[27] F. Mei, G. Chen, L. Tian, S.-L. Zhu, and S. Jia, Robust quantum state transfer via topological edge states in superconducting qubit chains, Phys. Rev. A **98**, 012331 (2018).
[28] S. Longhi, Topological pumping of edge states via adiabatic passage, Phys. Rev. B **99**, 155150 (2019).
[29] S. Longhi, G. L. Giorgi, and R. Zambrini, Landau–Zener topological quantum state transfer, Adv. Quantum Technol. **2**, 1800090 (2019).
[30] L.-N. Zheng, L. Qi, L.-Y. Cheng, H.-F. Wang, and S. Zhang, Defect-induced controllable quantum state transfer via a topologically protected channel in a flux qubit chain, Phys. Rev. A **102**, 012606 (2020).
[31] L. Qi, G.-L. Wang, S. Liu, S. Zhang, and H.-F. Wang, Engineering the topological state transfer and topological beam splitter in an even-sized Su-Schrieffer-Heeger chain, Phys. Rev. A **102**, 022404 (2020).
[32] F. M. D'Angelis, F. A. Pinheiro, D. Guéry-Odelin, S. Longhi, and F. m. c. Impens, Fast and robust quantum state transfer in a topological Su-Schrieffer-Heeger chain with next-to-nearest-neighbor interactions, Phys. Rev. Res. **2**, 033475 (2020).
[33] N. E. Palaiodimopoulos, I. Brouzos, F. K. Diakonos, and G. Theocharis, Fast and robust quantum state transfer via a topological chain, Phys. Rev. A **103**, 052409 (2021).
[34] J. Cao, W.-X. Cui, X. X. Yi, and H.-F. Wang, Controllable photon-phonon conversion via the topologically protected edge channel in an optomechanical lattice, Phys. Rev. A **103**, 023504 (2021).
[35] J. Yuan, C. Xu, H. Cai, and D.-W. Wang, Gap-protected transfer of topological defect states in photonic lattices, APL Photonics **6**, 030803 (2021).
[36] L. Qi, Y. Yan, Y. Xing, X.-D. Zhao, S. Liu, W.-X. Cui, X. Han, S. Zhang, and H.-F. Wang, Topological router induced via long-range hopping in a Su-Schrieffer-Heeger chain, Phys. Rev. Res. **3**, 023037 (2021).
[37] C. Wang, L. Li, J. Gong, and Y.-x. Liu, Arbitrary entangled state transfer via a topological qubit chain, Phys. Rev. A **106**, 052411 (2022).
[38] L.-N. Zheng, X. Yi, and H.-F. Wang, Engineering a phase-robust topological router in a dimerized superconducting-circuit lattice with long-range hopping and chiral symmetry, Phys. Rev. Appl. **18**, 054037 (2022).
[39] Y. Miyazawa, C.-W. Chen, R. Chaunsali, T. S. Gormley, G. Yin, G. Theocharis, and J. Yang, Topological state transfer in Kresling origami, Commun Mater **3**, 62 (2022).
[40] W. Liu, C. Wu, Y. Jia, S. Jia, G. Chen, and F. Chen, Observation of edge-to-edge topological transport in a photonic lattice, Phys. Rev. A **105**, L061502 (2022).
[41] D.-W. Wang, C. Zhao, J. Yang, Y.-T. Yan, and L. Zhou, Simulating the extended Su-Schrieffer-Heeger model and transferring an entangled state based on a hybrid cavity-magnon array, Phys. Rev. A **107**, 053701 (2023).
[42] X. Zhao, Y. Xing, J. Cao, S. Liu, W.-X. Cui, and H.-F. Wang, Engineering quantum diode in one-dimensional time-varying superconducting circuits, npj Quantum Inf **9**, 59 (2023).
[43] J. Zurita, C. E. Creffield, and G. Platero, Fast quantum transfer mediated by topological domain walls, Quantum **7**, 1043 (2023).
[44] S. V. Romero, X. Chen, G. Platero, and Y. Ban, Optimizing edge-state transfer in a Su-Schrieffer-Heeger chain via hybrid analog-digital strategies, Phys. Rev. Appl. **21**, 034033 (2024).
[45] J.-X. Han, J.-L. Wu, Z.-H. Yuan, Y.-J. Chen, Y. Xia, Y.-Y. Jiang, and J. Song, Fast and controllable topological excitation transfers in hybrid magnon-photon systems, Phys. Rev. Appl. **21**, 014057 (2024).
[46] T. Tian, H. Cai, L. Zhang, Y. Zhang, C.-K. Duan, and J. Zhou, Nonadiabatic topological transfer in a nanomechanical phononic lattice, Phys. Rev. B **109**, 125123 (2024).
[47] D. Fernández-Fernández, Y. Ban, and G. Platero, Flying spin qubits in quantum dot arrays driven by spin-orbit interaction, Quantum **8**, 1533 (2024).
[48] D.-W. Wang, C. Zhao, J. Yang, Y.-T. Yan, and L. Zhou, Controllable excitation transfer based on the coupling of an atom with a finite-size Su-Schrieffer-Heeger chain, Phys. Rev. A **109**, 033708 (2024).
[49] L.-N. Zheng, H.-F. Wang, and X. Yi, Robust entangled state transmission and preparation in a trimer-like chain, Chin. J. Phys. **93**, 471 (2025).
[50] M. Kohmoto, L. P. Kadanoff, and C. Tang, Localization problem in one dimension: Mapping and escape, Phys. Rev. Lett. **50**, 1870 (1983).
[51] S. Ostlund, R. Pandit, D. Rand, H. J. Schellnhuber, and E. D. Siggia, One-dimensional Schrödinger equation with an almost periodic potential, Phys. Rev. Lett. **50**, 1873 (1983).
[52] D. Levine and P. J. Steinhardt, Quasicrystals: A new class of ordered structures, Phys. Rev. Lett. **53**, 2477 (1984).
[53] D. Shechtman, I. Blech, D. Gratias, and J. W. Cahn, Metallic phase with long-range orientational order and no translational symmetry, Phys. Rev. Lett. **53**, 1951 (1984).
[54] M. Kohmoto, B. Sutherland, and K. Iguchi, Localization of optics: Quasiperiodic media, Phys. Rev. Lett. **58**, 2436 (1987).
[55] J. M. Luck, Cantor spectra and scaling of gap widths in deterministic aperiodic systems, Phys. Rev. B **39**, 5834 (1989).
[56] A. I. Goldman and R. F. Kelton, Quasicrystals and crystalline approximants, Rev. Mod. Phys. **65**, 213 (1993).
[57] D. Tanese, E. Gurevich, F. Baboux, T. Jacqmin, A. Lemaître, E. Galopin, I. Sagnes, A. Amo, J. Bloch, and E. Akkermans, Fractal energy spectrum of a polariton gas in a fibonacci quasiperiodic potential, Phys. Rev. Lett. **112**, 146404 (2014).
[58] M. Reisner, Y. Tahmi, F. Piéchon, U. Kuhl, and F. Mortessagne, Experimental observation of multifractality in Fibonacci chains, Phys. Rev. B **108**, 064210 (2023).
[59] A. Moustaj, M. Röntgen, C. V. Morfonios, P. Schmelcher, and C. Morais Smith, Spectral properties of two coupled fibonacci chains, New J. Phys. **25**, 093019 (2023).
[60] S. Franca, T. Seidemann, F. Hassler, J. van den Brink, and I. C. Fulga, Impedance spectroscopy of chiral symmetric topoelectrical circuits, Phys. Rev. B **109**, L241103 (2024).

[61] A. Jagannathan, The fibonacci quasicrystal: Case study of hidden dimensions and multifractality, Rev. Mod. Phys. **93**, 045001 (2021).

[62] O. Zilberberg, Topology in quasicrystals, Opt. Mater. Express **11**, 1143 (2021).

[63] Y. E. Kraus and O. Zilberberg, Topological equivalence between the Fibonacci quasicrystal and the Harper model, Phys. Rev. Lett. **109**, 116404 (2012).

[64] K. A. Madsen, E. J. Bergholtz, and P. W. Brouwer, Topological equivalence of crystal and quasicrystal band structures, Phys. Rev. B **88**, 125118 (2013).

[65] F. Flicker and J. van Wezel, Quasiperiodicity and 2D topology in 1D charge-ordered materials, Europhys. Lett. **111**, 37008 (2015).

[66] Y. E. Kraus and O. Zilberberg, Quasiperiodicity and topology transcend dimensions, Nature Phys **12**, 624 (2016).

[67] G. Rai, H. Schlömer, C. Matsumura, S. Haas, and A. Jagannathan, Bulk topological signatures of a quasicrystal, Phys. Rev. B **104**, 184202 (2021).

[68] J. Fan and H. Huang, Topological states in quasicrystals, Front. Phys. **17**, 13203 (2022).

[69] A. Jagannathan, Missing link between the two-dimensional quantum Hall problem and one-dimensional quasicrystals, Phys. Rev. B **112**, L100102 (2025).

[70] A. Dareau, E. Levy, M. B. Aguilera, R. Bouganne, E. Akkermans, F. Gerbier, and J. Beugnon, Revealing the topology of quasicrystals with a diffraction experiment, Phys. Rev. Lett. **119**, 215304 (2017).

[71] K. Singh, K. Saha, S. A. Parameswaran, and D. M. Weld, Fibonacci optical lattices for tunable quantum quasicrystals, Phys. Rev. A **92**, 063426 (2015).

[72] L. J. Splitthoff, M. C. Belo, G. Jin, Y. Liu, E. Greplova, and C. K. Andersen, Gate-tunable phase transition in a resonator-based Su-Schrieffer-Heeger chain, Phys. Rev. Res. **6**, 043286 (2024).

[73] P. D. Johannsen and C. Schrade, Fermionic quantum simulation on Andreev bound state superlattices, Phys. Rev. Res. **7**, 023153 (2025).

[74] M. Röntgen, C. V. Morfonios, R. Wang, L. Dal Negro, and P. Schmelcher, Local symmetry theory of resonator structures for the real-space control of edge states in binary aperiodic chains, Phys. Rev. B **99**, 214201 (2019).

[75] Z.-G. Chen, W. Tang, R.-Y. Zhang, Z. Chen, and G. Ma, Landau-Zener transition in the dynamic transfer of acoustic topological states, Phys. Rev. Lett. **126**, 054301 (2021).

[76] B. Chen, Y.-D. Peng, Y. Li, and X.-F. Qian, Robust multiple-range coherent quantum state transfer, Sci. Rep. **6**, 28886 (2016).

[77] S. A. Hill and W. K. Wootters, Entanglement of a pair of quantum bits, Phys. Rev. Lett. **78**, 5022 (1997).

[78] L. Mazzola, B. Bellomo, R. Lo Franco, and G. Compagno, Connection among entanglement, mixedness, and nonlocality in a dynamical context, Phys. Rev. A **81**, 052116 (2010).

[79] A. D. Greentree, J. H. Cole, A. R. Hamilton, and L. C. L. Hollenberg, Coherent electronic transfer in quantum dot systems using adiabatic passage, Phys. Rev. B **70**, 235317 (2004).

[80] D. Guéry-Odelin, A. Ruschhaupt, A. Kiely, E. Torrontegui, S. Martínez-Garaot, and J. G. Muga, Shortcuts to adiabaticity: Concepts, methods, and applications, Rev. Mod. Phys. **91**, 045001 (2019).

[81] Z. Fedorova, H. Qiu, S. Linden, and J. Kroha, Observation of topological transport quantization by dissipation in fast thouless pumps, Nat. Commun. **11**, 3758 (2020).

[82] D. Dreon, A. Baumgärtner, X. Li, S. Hertlein, T. Esslinger, and T. Donner, Self-oscillating pump in a topological dissipative atom–cavity system, Nature (London) **608**, 494 (2022).

[83] S. Diehl, A. Micheli, A. Kantian, B. Kraus, H. P. Büchler, and P. Zoller, Quantum states and phases in driven open quantum systems with cold atoms, Nature Phys **4**, 878 (2008).

[84] S. Diehl, E. Rico, M. A. Baranov, and P. Zoller, Topology by dissipation in atomic quantum wires, Nature Phys **7**, 971 (2011).

[85] J. C. Budich, P. Zoller, and S. Diehl, Dissipative preparation of chern insulators, Phys. Rev. A **91**, 042117 (2015).

[86] A. K. Ghosh and A. M. Black-Schaffer, Majorana zero-modes in a dissipative rashba nanowire, SciPost Phys. **17**, 036 (2024).

[87] F. Verstraete, M. M. Wolf, and J. Ignacio Cirac, Quantum computation and quantum-state engineering driven by dissipation, Nature Phys **5**, 633 (2009).

[88] X. Tang, T. Chen, and X. Zhang, Controlling transfer and chirality of topological quantum state through dissipation in quantum walk, Phys. Rev. Res. **7**, 013159 (2025).

[89] A. K. Ghosh, R. Seoane Souto, V. Azimi-Mousolou, A. Black-Schaffer, and P. Holmvall, Quantum state transfer and maximal entanglement between distant qubits using a minimal quasicrystal pump, Zenodo (2025), https://doi.org/10.5281/zenodo.17288531.